Available online at www.sciencedirect.com
SCIENCE DIRECT®
PERGAMON
International Journal of Heat and Mass Transfer 46 (2003) 3551–3572
International Journal of HEAT and MASS TRANSFER
www.elsevier.com/locate/ijhmt

Experimental benchmark data for turbulent natural convection in an air filled square cavity

F. Ampofo, T.G. Karayiannis *

Division of Environmental, Energy and Building Services Engineering, Faculty of Engineering, Science and Technology, South Bank University, 103 Borough Road, London SE1 0AA, UK

Received 11 September 2002; received in revised form 19 March 2003

Abstract

An experimental study of low-level turbulence natural convection in an air filled vertical square cavity was conducted. The cavity was 0.75 m high × 0.75 m wide × 1.5 m deep giving 2D flow. The hot and cold walls of the cavity were isothermal at 50 and 10 °C respectively giving a Rayleigh number of 1.58×10^9. The local velocity and temperature were simultaneously measured at different locations in the cavity and both mean and fluctuation quantities are presented, i.e. $\bar{u}$, u'_{rms}, $\bar{v}$, v'_{rms}, $\overline{T}$, T'_{rms}, $\overline{u'v'}$, $\overline{u'T'}$ and $\overline{v'T'}$. The local and average Nusselt numbers, the wall shear stress as well as the turbulent kinetic energy and the dissipation rate of the temperature variance are also presented. The experiments were conducted with very high accuracy and as such the results can form experimental benchmark data and will be useful for validation of computational fluid dynamics codes.

Keywords: Natural convection; Velocity distribution; Temperature distribution; Heat transfer; Wall shear stress; Turbulence quantities

1. Introduction

Natural convection in enclosures is of importance in many engineering applications. These include energy transfer in rooms and buildings, nuclear reactor cooling, solar collectors and electronic equipment cooling. Natural convection in a rectangular cavity is also a very good vehicle for both experimental and theoretical studies. In experimental terms, the geometry of the rectangular cavity is simple and its boundary conditions are relatively easy to assess so that researchers can focus on the measurements of important quantities such as velocity and temperature profiles. In numerical terms, the flow phenomena in the cavity are complicated and plentiful that they intrigue both physicists and engineers. However, in spite of the developments in the measurement technology and instruments, as well as in numerical methods and computers, fully describing the fluid flow and heat transfer in such a geometry still remains a challenge. In experimental studies, the flow is very sensitive to the experimental conditions. Further, boundary conditions on the horizontal cavity surfaces, defined in numerical work as adiabatic or perfectly conducting, are not easily realised in experiments, e.g. in a water filled cavity, the thermal boundary conditions on these surfaces lie somewhere in between the above two limiting cases [1]. Different fluids, e.g. air and water may exhibit significantly different temperature and fluid flow patterns in cavities of similar dimensions [2]. Although, convection in enclosures has been extensively studied experimentally, almost all the past researchers measured the velocity and temperature profiles separately. This prevented them from studying the velocity–temperature correlations, $\overline{u'_i T'}$, in enclosures which are needed to understand better how the heat transfer is affected by flow characteristics and physical parameters such as free stream turbulence, pressure gradients and rough walls. These experimental data are also needed for the successful modelling of turbulent flows. The simultaneous measurement of local velocity and temperature is quite difficult. Some of the difficulty arises from the fact that in

* Corresponding author. Tel.: +44-207-815-7628; fax: +44-208-815-7699.
E-mail address: karayitg@sbu.ac.uk (T.G. Karayiannis).

0017-9310/03/$ - see front matter © 2003 Elsevier Ltd. All rights reserved.
doi:10.1016/S0017-9310(03)00147-9

Nomenclature

A	heat transfer area (m^2)
AR_x	aspect ratio, $AR_x = H/L$
AR_z	aspect ratio for z-direction $AR_x = D/L$
C_μ	empirical constant in turbulence models
D	depth of the cavity (m)
g	gravitational acceleration (m/s^2)
h	average convective heat transfer coefficient, $h = Q/A(T_w - T_a)$ (W/m^2 K)
h_j	subgrid-scale heat fluxes (m K/s)
H	height of the cavity (m)
k	thermal conductivity (W/m K)
k	turbulent kinetic energy (m^2/s^2)
l	turbulence length scale (m)
L	width of the cavity (m)
m	any variable
n	any variable
Nu	local Nusselt number, $Nu = hL/k$
Pr	Prandtl number, $Pr = v/\alpha$
Q	rate of heat transfer (W)
Ra	Rayleigh number, $Ra = g\beta(T_h - T_c)L^3/(\alpha v)$
Ra_H	Rayleigh number based on height, $Ra_H = g\beta(T_h - T_c)H^3/(\alpha v)$
$\overline{S}_{ij}$	large-scale strain rate (s^{-1})
T	temperature (°C, K)
u	fluid velocity component in x-direction (m/s)
$\overline{u'v'}$	Reynolds stress (m^2/s^2)
$\overline{u_i'T'}$	turbulent heat flux (m K/s)
v	fluid velocity component in y-direction (m/s)
V_o	buoyancy velocity, $V_o = \sqrt{g\beta H \Delta T}$ (m/s)
w	fluid velocity component in z-direction (m/s)
x	displacement in x-direction (m)
x, y, z	Cartesian co-ordinates
X, Y, Z	dimensionless co-ordinates
ΔT	temperature difference $\Delta T = T_h - T_c$ (K)

Greek symbols

α	thermal diffusivity (m^2/s)
β	thermal expansion coefficient (1/K)
δ_{ij}	Kronecker delta function ($\delta_{ij} = 1$ if $i = j$ and $\delta_{ij} = 0$ if $i \neq j$)
ε	turbulent energy dissipation rate (m^2/s^3)
η	Kolmogorov length scale (m)
μ	dynamic viscosity (kg/m s)
v	kinematic viscosity (m^2/s)
ρ	fluid density (kg/m^3)
τ_{ij}	turbulent stress tensor (m^2/s^2)

Superscripts

–	average value
′	fluctuation component

Subscripts

b	bottom wall
c	cold wall
e	ambient
h	hot wall
i	arbitrary quantity
o	reference condition
t	top wall
w	wall
rms	root mean square
SGS	subgrid-scale

most flows, the size of the smallest significant turbulent eddy is much less than the closest separation at which velocity and temperature probes can be used without interfering with one another. In principle, it is possible to make the measurement using a multi-sensor hot- and cold-wire anemometry system since that instrument responds to both temperature and velocity. In practice, however, the use of multi-sensor probes has three distinct disadvantages: firstly, interference effects among the prongs and/or sensors may be present; secondly, the hot-wire data may need to be corrected when using it in a heated fluid medium and thirdly, the errors involved in extracting the values of turbulence heat flux from the instrument signals tend to be unacceptably large. Also, the accuracy of measuring the temperature fluctuations is limited by the frequency response of the sensor.

An experimental study of heat transfer and fluid flow in a standard air filled square cavity was conducted in this study. The local velocity and temperature were simultaneously measured at different locations in the cavity using a laser Doppler anemometer (LDA) and a micro-diameter thermocouple. This helped eliminate the above-mentioned problems associated with a multi-sensor hot- and cold-wire anemometry system. The study aimed to provide highly accurate turbulent convection data, which can provide further insight into the turbulent heat transfer in natural convection in enclosures and be used for the validation of computational fluid dynamics (CFD) codes.

2. Experimental facility and procedure

The experimental rig, see Fig. 1(a), used in the present study is fully automatically controlled. The major subsystems of the rig are the temperature control system, the cavity, and a facility for measuring the air velocity and temperature simultaneously. The temperature

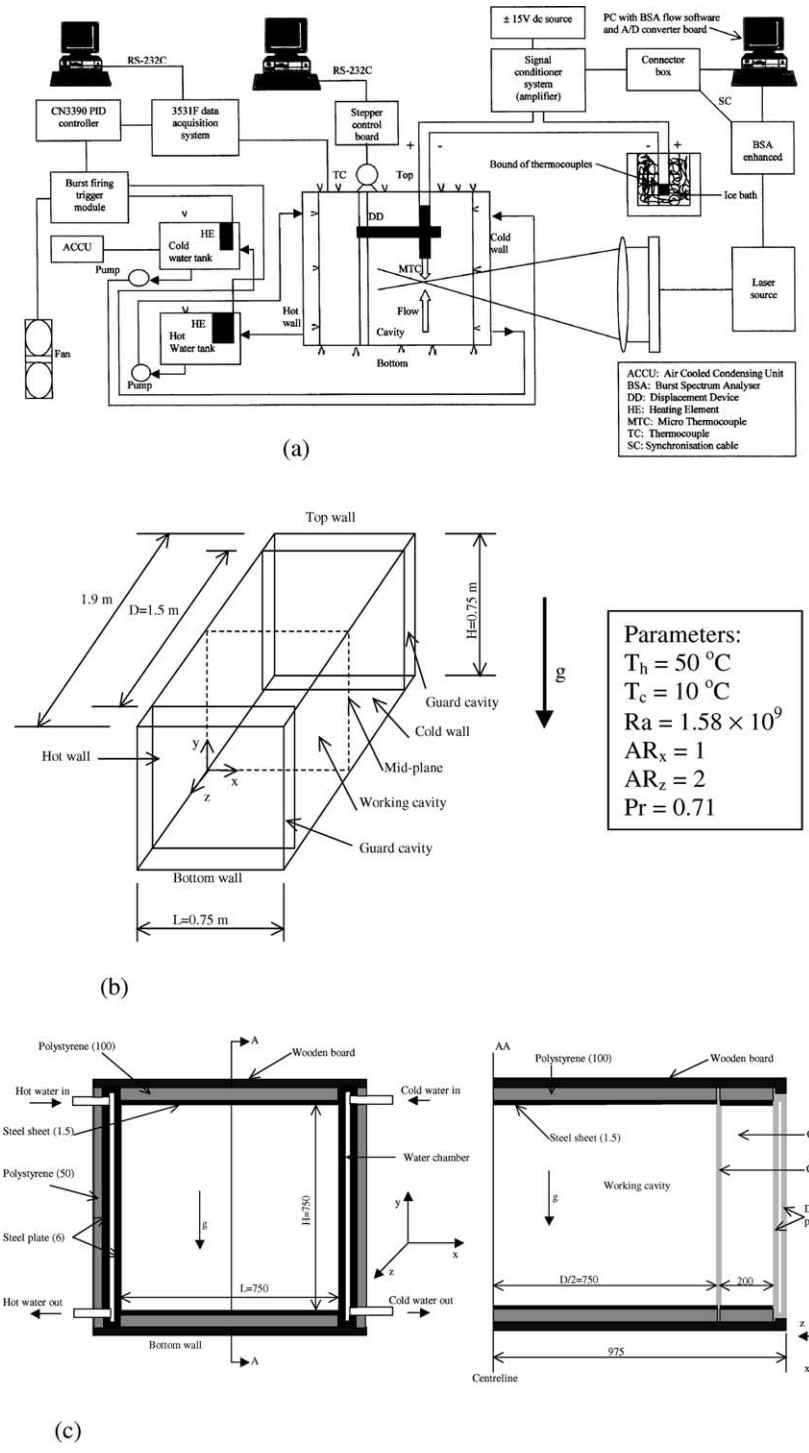

Fig. 1. Schematic diagram of the experimental facility and test cavity: (a) experimental facility, (b) three-dimensional schematic diagram of the air filled cavity and (c) the test cavity indicating detail of construction (all measurements are in mm).

control system comprised of a PC, a Schlumberger 3531F data acquisition system, a multi-loop proportional–integral–differential (PID) temperature-process controller and low noise K-type thermocouples. It

maintained a constant temperature water flow to chambers attached to the hot and cold plates, see Fig. 1(c). The PC, which controlled the Schlumberger 3531F data acquisition system, recorded the thermocouple readings and sent the signal to the PID controller. The PID controller then sent pulses to the burst firing trigger modules to alter the heating power, i.e. the power was either switched on or off at zero voltage. The cold and hot water streams were pumped through the water chambers at a rate of 40 l/min and at predetermined temperatures. The test cavity, shown in Fig. 1(b) and (c), was 0.75 m high $\times$ 0.75 m wide $\times$ 1.5 m deep. The hot and cold walls of the cavity were made of 6 mm mild steel plate. The hot wall was maintained isothermal at 50 ± 0.15 °C whilst the cold wall at 10 ± 0.15 °C giving a Ra of 1.58×10^9. The top and bottom walls were made from 1.5 mm mild steel sheet and provided highly conducting boundaries. The temperatures on these isothermal and horizontal walls were measured using K-type thermocouples. Two guard cavities surrounded the passive vertical walls to reduce the heat exchange with the ambient. The room temperature was controlled at 30 ± 0.2 °C. This was equal to the cavity average temperature (average of hot and cold walls temperatures).

Penot and N'Dame [3] pointed out that the 2D approximation of experimental natural convection in cavities should be valid if the horizontal aspect ratio (AR_z) of the cavity is greater than 1.8. In this study, AR_z was 2 and hence the depth of the cavity resulted in a 2D flow in the mid-plane of the cavity. Also, as stated earlier, we had two guard cavities on each side of the passive vertical walls. In addition, the average temperature of hot and cold walls was the same as ambient and the cavity was insulated. Hence the heat exchange between the cavity and environment was kept to a minimum. The 2D of the flow was also thoroughly examined and verified by the earlier work of Tian and Karayiannis [4,5] carried out in the same cavity. They measured and compared velocity distribution at three cavity depths, $Z = 0$, 0.533 and 0.8. The three profiles differed by only 4% on the peak velocity and 0.5 mm on its position, which proved that the depth of the cavity, the guard cavities and the ambient of 30 °C provided a 2D flow, especially at cavity centre.

The simultaneous measurements of local velocity and temperature are quite difficult and as stated earlier, some of the difficulty arises from the fact that in most flows the size of the smallest significant turbulent eddy is much less than the closest separation at which velocity and temperature probes can be used without interfering with one another. In view of this, it was very important to estimate the turbulent length scale correctly so as to reduce this interference between the probes to the minimum. The Kolmogorov length scale for small eddies, $\eta = (\nu^3/\varepsilon)^{1/4}$ [6], was used to estimate the maximum separation between the temperature and velocity probes. The dissipation rate, ε, of turbulent kinetic energy, k, was estimated from the relation between the turbulence length scale, l, k and ε, i.e.

$$\varepsilon = C_\mu^{3/4} k^{3/2}/l \tag{1}$$

where $C_\mu = 0.09$ [7]. The turbulence kinetic energy, k, is given as

$$k = \tfrac{1}{2}(\overline{u'^2} + \overline{v'^2} + \overline{w'^2}) \tag{2}$$

In this study, the flow is two-dimensional at the mid-section ($AR_z = 2$) and as such $\bar{w} = 0$. Cebeci and Bradshaw [8] reported that in isotropic turbulent flow, w' is of the same order as u' and v' even if $\bar{w} = 0$. In this anisotropic turbulent natural convection, it is very difficult to estimate w' without direct measurements. The experimental and numerical works of Kreplin and Eckelmann [9] and Spalart [10] respectively suggest that along an isothermal vertical wall the following relationship exists:

$$\overline{u'^2} \leqslant \overline{w'^2} \leqslant \overline{v'^2} \tag{3}$$

As a first estimation, we can use

$$\overline{w'^2} = \frac{\overline{u'^2} + \overline{v'^2}}{2} \tag{4}$$

i.e. the turbulent fluctuation in the z-direction contributes one third of the k. Therefore,

$$k = \frac{1.5(\overline{u'^2} + \overline{v'^2})}{2} \tag{5}$$

An initial measurement of the velocity distribution at mid-height of the cavity was used to estimate the turbulent kinetic energy which peaked near the hot wall at $\sim 4.5 \times 10^{-3}$ m^2/s^2. The velocity distribution was used to estimate l. At about cavity mid-height, the experimental results gave a boundary layer thickness of $\sim$5 mm and this value was used for l. Eq. (1) then gives $\varepsilon \approx 10^{-2}$ W/kg. The corresponding value of η is $\sim$0.4 mm. Therefore, the distance between the temperature and velocity probes in the present study was around 0.4 mm. An E-type thermocouple of wire diameter 25.4 μm was carried by a computer controlled two-dimensional displacement device (accurate to 0.1 mm) and was used to measure the temperature in the cavity with an accuracy of 0.1 K. The response time of the 25.4 μm thermocouple is 20 Hz in still air. The choice of thermocouple was based on the experimental work of Mergui and Penot [11], who stated that the highest turbulent frequency is less than 5 Hz in an air filled cavity ($Ra = 2.33 \times 10^9$, $AR_x = 0.9$). Thus, this thermocouple was sufficiently responsive to the high frequencies in this air cavity flow. A back scatter, two-dimensional LDA with a burst spectrum analyser and a 40 MHz frequency shift Bragg cell was used in the velocity measurements in the cavity. The laser source was a 300 mW argon laser. The measured velocity range was

from −0.5082 to +0.5082 m/s with a resolution of 6.20e−5 m/s and at a bandwidth of 0.125 MHz. The laser beams entered the cavity through the guard cavity at an angle of 3.5° to the isothermal wall. A front lens with a focal length of 1200 mm was used. The probe volume dimensions were 0.31 mm (diameter) × 9.8 mm (length). Incense smoke was used as seeding, which lasted for more than 24 h. The velocity was measured with an accuracy of 0.07%. The simultaneous velocity and temperature measurements were made by placing the LDA probe volume immediately upstream of the thermocouple wire at a distance of around 0.4 mm. The analogue to digital (A/D) board used to sample the temperature signal was set to start sampling at the same time as the LDA processors and also the A/D data and the LDA data were synchronised. Preliminary experiments were conducted at different times, at mid-height ($Y = y/L = 0.50$) across the cavity, to check among other things the influence of the measuring volume (LDA probe) on the thermocouple probe for the temperature measurements. The results showed that the influence of the measuring volume (LDA probe) on the thermocouple probe for the temperature measurements was negligible and that the repeatability for the various parameters measured was very good. The maximum deviation between readings obtained during experiments performed at different times was 0.5 K for the temperature and 2 mm/s for the velocity, see Ampofo [12] for further details. Also, the velocity and temperature results from the preliminary experiments were compared, with excellent agreement, to the earlier work of Tian and Karayiannis [4,5] carried out in the same cavity but with a different approach. The velocity and temperature profiles were measured separately in that study and hence they did not report any heat flux measurements. Tian and Karayiannis compared their results with the work of past researchers like Mergui et al. [13], Lankhorst [14], Beghein et al. [15], Ziai [16], King [17] and Paolucci [18]. The authors found that compared with earlier results, the agreement on the Nusselt number was good. Acceptable agreement was also found when comparing the temperature and velocity profiles at mid-height. Differences were found along the mid-width and the change rates of velocity and temperature along the walls. These comparisons will not be repeated in this paper since, as mentioned above, the present data agree with [4,5]. In the present work, 10 000 velocity and temperature samples were acquired simultaneously at the mid-plane of the cavity, see Fig. 1(b), for every point and the mean, root mean square and cross-correlation quantities were calculated as follows:

The mean quantities ($\overline{T}$, $\bar{u}$, $\bar{v}$)

$$\bar{m} = \frac{1}{N}\sum_{i=1}^{N} m_i \tag{6}$$

Table 1
Summary of uncertainties in the measured and estimated parameters

Parameter	Degree of uncertainty
Wall temperature	0.15 K
Air temperature	0.10 K
Air velocity	0.07%
Reynolds stress	0.10%
Turbulent heat flux	0.15%
Rayleigh number	0.62%
Nusselt number	0.25–1.13%
Wall shear stress	1.38%

The root mean square quantities ($T'_{\mathrm{rms}}, u'_{\mathrm{rms}}, v'_{\mathrm{rms}}$)

$$m'_{\mathrm{rms}} = \left[\frac{1}{N}\sum_{i=1}^{N}(m_i - \bar{m})^2\right]^{1/2} \tag{7}$$

The cross-correlation quantities ($\overline{u'v'}, \overline{u'T'}, \overline{v'T'}$)

$$\overline{m'n'} = \sum_{i=1}^{N}(m_i - \bar{m})(n_i - \bar{n}) \tag{8}$$

N is the number of readings taken in the experiments—10 000 in this study. The choice of the total number of samples acquired was based on the experimental work of Wardana et al. [19] who proved that the uncertainty of a statistical value decreases with increasing number of samples, and the uncertainty becomes less than ±5% when the number of samples is over 5000. All the measurements were taken at steady conditions at the mid-plane of the cavity on a fine non-uniform mesh. The authors performed an energy balance for the cavity. On the whole, heat transfer into the cavity from the hot and bottom walls was 98.12 and 21.67 W respectively. The net loss from the cold and top walls was 97.77 and 22.53 W respectively. The percentage error of heat input and output in the whole cavity was less than 0.5%. Table 1 gives a summary of the uncertainties in the measured and estimated parameters in this study. For further details on error analysis (bias and precision errors) and propagation see Ampofo [12].

3. Experimental results

One of the objectives of the study was to provide highly accurate turbulent convection data, which can be used for the validation of CFD codes. In view of this, the numerical values of the experimental results, $\bar{v}$, v'_{rms}, $\bar{u}$, u'_{rms}, $\overline{T}$, T'_{rms}, $\overline{u'v'}$, $\overline{u'T'}$, $\overline{v'T'}$, k, at the mid-height of the cavity are included in this paper, see Table 2, for easy assess and comparison with CFD results. Tables 3–6 also present the experimental results for wall shear stress, mean temperature distribution on the horizontal cavity walls, mean temperature distribution along the

Table 2
Experimental results at $Y = 0.5$ in the cavity

X	$\frac{\bar{v}}{V_0}$	$\frac{\bar{u}}{V_0}$	$\frac{v'_{\rm rms}}{V_0}$	$\frac{u'_{\rm rms}}{V_0}$	$\frac{\overline{T}-T_c}{\Delta T}$	$\frac{T'_{\rm rms}}{\Delta T}$	$\frac{\overline{u'v'}}{V_0^2}$	$\frac{\overline{v'T'}}{V_0\,\Delta T}$	$\frac{\overline{u'T'}}{V_0\,\Delta T}$	$\frac{k}{V_0^2}$
0.0000	0.0000	0.0000	0.0000	0.0000	1.0000	0.0000	0.0000	0.0000	0.0000	0.0000
3.3333e−4	0.0403	−3.6440e−4	3.9900e−4	2.6400e−4	0.9525	0.0164	−2.0000e−6	8.1925e−7	1.8250e−6	1.7167e−7
6.6667e−4	0.0611	−4.0890e−4	2.3880e−3	3.8600e−4	0.9300	0.0204	−4.0000e−6	2.0693e−6	4.3250e−6	4.3887e−6
1.0000e−3	0.0843	−4.1192e−4	7.5980e−3	1.0700e−3	0.9200	0.0288	−7.0000e−6	2.6700e−6	8.6000e−6	4.4156e−5
1.3333e−3	0.1001	−6.9210e−4	0.0205	4.9570e−3	0.9125	0.0345	−6.0300e−6	5.1933e−5	1.5310e−5	3.3442e−4
1.6667e−3	0.1158	−7.5100e−4	0.0201	5.2520e−3	0.8750	0.0391	−7.0000e−6	7.2950e−5	2.7483e−5	3.2409e−4
2.0000e−3	0.1325	−8.1300e−4	0.0283	6.4380e−3	0.8685	0.0453	−7.5000e−6	8.8798e−5	9.1600e−6	6.3269e−4
2.3333e−3	0.1457	−8.6300e−4	0.0296	6.8920e−3	0.8373	0.0548	−8.0000e−6	1.1604e−4	3.6800e−5	6.9266e−4
2.6667e−3	0.1613	−6.3400e−4	0.0359	7.7500e−3	0.8298	0.0586	−1.0000e−5	2.3725e−4	4.9525e−5	1.0098e−3
3.0000e−3	0.1655	−7.4700e−4	0.0378	8.8760e−3	0.8071	0.0585	−1.3200e−5	5.2205e−4	7.6475e−5	1.1330e−3
3.3333e−3	0.1739	−6.6700e−4	0.0396	9.0360e−3	0.7830	0.0620	−8.0000e−6	1.3910e−3	1.2780e−4	1.2349e−3
3.6667e−3	0.1831	5.7000e−4	0.0406	0.0109	0.7701	0.0629	−2.0000e−6	2.1665e−3	1.8410e−4	1.3236e−3
4.0000e−3	0.2000	6.4600e−4	0.0457	0.0116	0.7635	0.0669	1.4000e−5	2.8213e−3	2.2600e−4	1.6656e−3
6.6667e−3	0.2127	1.7600e−4	0.0651	0.0178	0.6793	0.0753	2.0000e−4	3.0438e−3	2.5590e−4	3.4158e−3
9.3333e−3	0.2081	3.2140e−3	0.0705	0.0270	0.6186	0.0658	4.0000e−4	2.7488e−3	2.7545e−4	4.2732e−3
0.0133	0.1745	4.6790e−3	0.0717	0.0281	0.5655	0.0527	6.0000e−4	2.5878e−3	2.4818e−4	4.4506e−3
0.0200	0.1308	4.7330e−3	0.0681	0.0306	0.5270	0.0327	9.7300e−4	1.9623e−3	1.7593e−4	4.1770e−3
0.0267	0.0918	3.8240e−3	0.0624	0.0323	0.5171	0.0256	1.0550e−3	8.5705e−4	1.2693e−4	3.6992e−3
0.0333	0.0620	3.2180e−3	0.0560	0.0343	0.5098	0.0186	1.0870e−3	2.5128e−4	7.0375e−5	3.2332e−3
0.0400	0.0374	−2.6610e−3	0.0443	0.0298	0.5045	0.0172	8.0000e−4	−8.4875e−5	8.9250e−6	2.1383e−3
0.0533	0.0130	−2.4680e−3	0.0371	0.0263	0.5149	0.0167	5.0000e−4	−1.6765e−4	−1.7425e−5	1.5471e−3
0.0667	2.8710e−3	−3.2530e−3	0.0230	0.0208	0.5175	0.0131	3.0000e−4	−5.2150e−5	−3.8650e−5	3.3113e−4
0.0800	2.1470e−3	−3.6510e−3	0.0165	0.0106	0.5313	9.1302e−3	3.8000e−5	−4.7125e−6	−5.4675e−5	2.8862e−4
0.1067	2.6300e−4	−3.3230e−3	0.0108	8.3850e−3	0.5375	7.8789e−3	−1.1000e−5	2.3270e−5	−1.4550e−5	1.4060e−4
0.1333	3.7280e−4	−2.3600e−3	9.8790e−3	7.3030e−3	0.5400	5.3791e−3	−1.0000e−6	1.9900e−6	−1.2750e−6	1.1320e−4
0.1600	3.7200e−4	−1.6450e−3	7.7750e−3	6.6490e−3	0.5236	3.3575e−3	3.0000e−6	−1.5575e−6	−8.5000e−7	7.8495e−5
0.2000	3.9700e−4	−1.1380e−3	7.7490e−3	4.9050e−3	0.5270	3.0334e−3	1.3000e−6	4.9950e−6	−9.0000e−7	6.3080e−5
0.2400	3.3100e−3	−1.0910e−3	7.5590e−3	4.8580e−3	0.5251	2.8629e−3	1.50000−6	4.0150e−7	−9.0000e−7	6.0554e−5
0.2800	2.7900e−4	−1.2860e−3	7.4410e−3	4.0490e−3	0.5277	2.9035e−3	1.6000e−6	1.0933e−6	−2.2500e−7	5.3822e−5
0.3200	1.7200e−4	−9.7800e−4	7.1790e−3	4.1550e−3	0.5308	3.2389e−3	2.0000e−6	−1.5413e−6	1.7000e−6	5.1602e−5
0.3600	1.1100e−4	−5.8400e−4	6.5000e−3	4.3470e−3	0.5280	3.1980e−3	1.0000e−6	−2.2993e−6	−6.2500e−7	4.5860e−5
0.4000	1.8100e−4	5.1000e−4	6.1530e−3	3.9160e−3	0.5217	2.8874e−3	−1.0000e−6	−2.1257e−7	−2.0000e−7	3.9896e−5
0.4400	−1.2700e−4	6.3800e−4	5.4530e−3	4.0150e−3	0.5200	2.9203e−3	−2.0000e−6	−3.4800e−7	1.0000e−7	3.4392e−5
0.5000	−6.9000e−5	5.7900e−4	5.0290e−3	5.1590e−3	0.5174	3.1881e−3	1.1000e−6	8.7250e−7	1.0325e−6	3.8930e−5
0.5600	−4.8700e−4	1.0660e−3	4.4400e−3	5.0040e−3	0.5188	3.1007e−3	−2.8000e−6	1.4750e−5	1.1250e−6	3.3565e−5

0.6000	−1.8100e−4	1.7850e−3	4.4200e−3	4.1250e−3	0.5154	4.8337e−3	−2.0000e−6	−2.3500e−6	1.1500e−6	2.7414e−5
0.6400	−6.0600e−4	2.1460e−3	4.5170e−3	4.1350e−3	0.5165	4.0352e−3	−2.0000e−6	5.0000e−7	−4.2500e−7	2.8126e−5
0.6800	−4.9400e−4	2.3670e−3	4.4180e−3	3.4520e−3	0.5190	3.0430e−3	−3.0000e−6	7.1250e−6	2.0000e−7	2.3576e−5
0.7200	−4.9900e−4	2.4850e−3	4.8540e−3	3.3290e−3	0.5202	3.3391e−3	−2.0000e−6	6.5500e−7	−7.5000e−8	2.5983e−5
0.7600	−4.5800e−4	2.5830e−3	4.7060e−3	3.4520e−3	0.5160	4.3246e−3	−1.0000e−6	6.3500e−6	−9.3250e−6	2.5547e−5
0.8000	−2.2700e−4	3.4510e−3	4.6640e−3	3.6450e−3	0.5135	7.0418e−3	−1.0000e−6	7.0000e−7	−5.0000e−7	2.6279e−5
0.8400	−2.4900e−4	3.1830e−3	4.9470e−3	4.0910e−3	0.5138	5.0101e−3	−1.0000e−6	−5.3500e−6	−3.6750e−6	3.0907e−5
0.8667	−3.1700e−4	3.3130e−3	5.1190e−3	4.3730e−3	0.5079	6.5627e−3	−6.0000e−7	3.5250e−6	−3.9000e−6	3.3995e−5
0.8933	1.2600e−3	2.9930e−3	8.0740e−3	6.6590e−3	0.5076	5.8379e−3	−2.7000e−5	−3.9250e−6	−1.2450e−5	8.2149e−5
0.9200	4.4080e−3	2.8370e−3	0.0156	0.0151	0.5061	7.7054e−3	3.5000e−5	−3.7525e−5	−3.6425e−5	3.5210e−4
0.9333	2.7420e−3	1.9950e−3	0.0245	0.0156	0.5151	0.0115	1.0000e−5	−6.5450e−5	3.7775e−5	6.3357e−4
0.9467	−0.0108	1.3280e−3	0.0352	0.0223	0.5257	0.0147	3.5700e−4	−8.3900e−5	6.7250e−5	1.2997e−3
0.9600	−0.0403	−2.2620e−3	0.0465	0.0254	0.5198	0.0166	5.9600e−4	−9.9100e−5	7.0725e−5	2.1030e−3
0.9667	−0.0684	−4.3800e−3	0.0559	0.0286	0.5313	0.0166	8.7000e−4	3.5020e−4	8.0750e−5	2.9600e−3
0.9733	−0.0916	−5.3000e−3	0.0639	0.0310	0.5199	0.0248	9.9300e−4	5.8808e−4	1.3713e−4	3.7844e−3
0.9800	−0.1252	−5.1300e−3	0.0661	0.0272	0.5047	0.0353	9.4400e−4	1.0818e−3	1.87780−4	3.8323e−3
0.9867	−0.1828	−4.9900e−3	0.0652	0.0224	0.4556	0.0550	6.4700e−4	2.0298e−3	2.4098e−4	3.5665e−3
0.9907	−0.2185	−4.6620e−3	0.0659	0.0183	0.3834	0.0703	−3.3000e−4	2.7414e−3	1.5248e−4	3.5079e−3
0.9933	−0.2257	−2.7390e−3	0.0586	0.0158	0.3137	0.0565	2.0900e−4	2.4064e−3	1.18000−4	2.7624e−3
0.9960	−0.1884	−1.5920e−3	0.0429	0.0106	0.2434	0.0572	1.0000e−6	1.9478e−3	7.0950e−5	1.4673e−3
0.9963	−0.1803	−1.5680e−3	0.0404	9.8470e−3	0.2318	0.0519	8.0000e−7	1.6570e−3	6.11500−5	1.2987e−3
0.9967	−0.1736	−1.4050e−3	0.0382	8.6060e−3	0.2136	0.0465	−4.0000e−6	8.2023e−4	5.8625e−5	1.1511e−3
0.9970	−0.1604	−1.4560e−3	0.0355	7.4360e−3	0.2050	0.0423	−6.0000e−6	5.0158e−4	3.6425e−5	9.8586e−4
0.9973	−0.1488	−8.6500e−4	0.0326	6.6200e−3	0.1865	0.0361	−2.3000e−5	4.1465e−4	3.4300e−5	8.3190e−4
0.9977	−0.1268	−6.8500e−4	0.0309	5.8210e−3	0.1608	0.0308	−1.4000e−5	3.7715e−4	3.0850e−5	7.4138e−4
0.9980	−0.1056	−5.1000e−4	0.0277	5.0320e−3	0.1324	0.0297	−6.0000e−6	2.7485e−4	1.6625e−5	5.9591e−4
0.9983	−0.0835	−4.3900e−4	0.0230	4.7780e−3	0.1183	0.0230	−2.0000e−6	1.3040e−4	1.5750e−5	4.1470e−4
0.9987	−0.0588	−3.9700e−4	0.0211	4.0410e−3	0.0935	0.0171	−1.0000e−6	3.6300e−5	1.4000e−5	3.4555e−4
0.9990	−0.0314	−1.9100e−4	0.0158	3.3280e−3	0.0777	0.0174	−1.0000e−6	−9.9750e−6	1.1500e−5	1.9592e−4
0.9993	−3.3890e−3	−2.2000e−5	0.0101	2.7850e−3	0.0657	0.0115	−1.0000e−6	−9.5250e−6	1.0200e−5	8.2340e−5
0.9997	−4.1200e−4	−1.2000e−5	8.1010e−3	7.8500e−4	0.0309	0.0105	−1.0000e−6	−9.4750e−6	8.0250e−6	4.9682e−5
1.0000	0.0000	0.0000	0.0000	0.0000	0.0000	0.0000	0.0000	0.0000	0.0000	0.0000

$X = x/L$, $Y = y/L$, $V_0 = \sqrt{g\beta H\,\Delta T} = 1$ m/s, $\Delta T = T_h - T_c = 40$ K.

Table 3
Wall shear stress

Hot wall		Cold wall	
Distance from bottom wall, Y	$\tau_w \times 10^3$ (N/m^2)	Distance from top wall, $1-Y$	$\tau_w \times 10^3$ (N/m^2)
0.0000	0.0000	1.0000	0.0000
0.0500	1.0600	0.9500	1.0800
0.1000	1.4400	0.9000	1.4200
0.2000	1.5600	0.8000	1.6500
0.3000	1.6200	0.7000	1.7000
0.4000	1.6600	0.6000	1.7600
0.5000	1.6400	0.5000	1.7200
0.6000	1.5200	0.4000	1.6000
0.7000	1.3000	0.3000	1.4000
0.8000	1.2000	0.2000	1.3000
0.9000	1.0800	0.1000	1.1000
0.9500	0.7000	0.0500	0.7500
1.0000	0.0000	0.0000	0.0000

$Y = y/L$.

Table 4
Mean temperature distribution on horizontal walls

X	$(\overline{T}-T_c)/\Delta T$	
	Top wall	Bottom wall
0.0000	1.0000	1.0000
2.0000e−3	0.9490	0.9184
6.6700e−3	0.9333	0.9038
0.0133	0.9342	0.8862
0.0267	0.9183	0.8639
0.0533	0.8782	0.7733
0.1000	0.8210	0.6608
0.2000	0.7597	0.5263
0.3000	0.7107	0.4520
0.4000	0.6779	0.3960
0.5000	0.6393	0.3503
0.6000	0.6135	0.3116
0.7000	0.5578	0.2722
0.8000	0.4880	0.2214
0.9000	0.3372	0.1490
0.9467	0.2338	0.0938
0.9733	0.1409	0.0445
0.9867	0.1334	0.0352
0.9933	0.1234	0.0272
0.9980	0.0967	0.0185
1.0000	0.0000	0.0000

$X = x/L$, $\Delta T = T_h - T_c = 40$ K.

cavity mid-width and local Nusselt number distribution along the walls of the cavity respectively. The experimental results at different heights of the cavity are also available from the authors. The general flow and thermal behaviour of the fluid in the cavity would not be presented in graphical form in this paper. Interested readers can consult Tian and Karayiannis [4,5] where such information is given. Instead, in this section, the experimental results in the immediate vicinity to the

Table 5
Mean temperature distribution along mid–width

$(\overline{T}-T_c)/\Delta T$	Y
0.3553	0.0000
0.3328	1.3333e−3
0.3253	2.6667e−3
0.3178	4.0000e−3
0.2978	6.6667e−3
0.2828	9.3333e−3
0.2778	0.0133
0.2737	0.0200
0.2790	0.0267
0.2814	0.0360
0.2906	0.0500
0.3086	0.0750
0.3250	0.1000
0.3571	0.1500
0.3804	0.2000
0.4001	0.2500
0.4213	0.3000
0.4395	0.3500
0.4564	0.4000
0.4854	0.4500
0.5174	0.5000
0.5463	0.5500
0.5662	0.6000
0.5800	0.6500
0.6068	0.7000
0.6234	0.7500
0.6356	0.8000
0.6644	0.8500
0.6825	0.9000
0.6991	0.9250
0.7182	0.9500
0.7250	0.9640
0.7300	0.9733
0.7375	0.9800
0.7350	0.9867
0.7250	0.9907
0.7125	0.9933
0.7000	0.9960
0.6850	0.9973
0.6635	0.9987
0.6443	1.0000

$Y = y/L$, $\Delta T = T_h - T_c = 40$ K.

isothermal vertical walls will be used to study the near-wall turbulence in the cavity. Also, the distribution of the turbulent heat flux in the cavity will be presented and discussed in detail being the first time it has been directly measured in an air filled square cavity at low-level turbulence.

3.1. Inner and outer boundary layer structures

A turbulent boundary layer can be described as a two-layer structure, namely an inner layer and an outer layer [20], separated by the position of the velocity

Table 6
Local Nusselt number distribution along the walls

Y	Nu		X	Nu	
	Hot wall	Cold wall		Bottom wall	Top wall
0.0200	136.0000	21.0000	0.0133	75.0000	22.0000
0.0493	122.0000	33.0000	0.0400	58.0000	18.0000
0.1000	95.0000	42.0000	0.0800	40.0000	8.0000
0.2000	84.0000	44.0000	0.1333	38.0000	5.0000
0.3000	72.0000	47.0000	0.2000	36.0000	2.0000
0.4000	65.0000	50.0000	0.2800	20.0000	−4.0000
0.5000	58.0000	60.0000	0.3600	16.0000	−8.0000
0.6000	52.0000	62.0000	0.5000	10.0000	−11.0000
0.7000	47.0000	69.0000	0.6400	8.0000	−18.0000
0.8000	40.0000	80.0000	0.7200	4.0000	−23.0000
0.9000	36.0000	87.0000	0.8000	1.0000	−31.0000
0.9493	28.0000	122.0000	0.8667	−12.0000	−35.0000
0.9867	17.0000	138.0000	0.9200	−15.0000	−42.0000
			0.9600	−19.0000	−55.0000
			0.9867	−25.0000	−70.0000

$X = x/L$, $Y = y/L$.

maximum. Fig. 2(a) shows the boundary layer structure (vertical velocity profile) along the hot wall in the cavity at $Y = 0.5$. The boundary layer on the cold wall is almost exactly anti-symmetrical. The inner layer is 5 mm wide (at $Y = 0.5$) and the outer layer is 75 mm wide, i.e. the inner layer is less than 7% of the outer layer. The thickness of the inner layer along the isothermal walls is not constant. It varies between 4 and 7 mm depending on the height along the isothermal walls. It is narrow at the bottom of the hot wall (and at the top of the cold wall) and wider at the top of the hot wall (and at the bottom of the cold wall). The inner layer can be divided further into a viscous layer next to the wall where the Reynolds stress is negligible and a buoyant sublayer for the rest of the inner layer, see Fig. 2(b). In the viscous layer, very close to the wall, the temperature profile is nearly linear and this region is referred to as conductive layer. The linearity of the temperature profile is shown in Fig. 2(b) with a line drawn through the measured points. In the conductive layer, the heat flux is constant [21]. The viscous layer is about 3 mm in this study with 2 mm of it being the conductive layer. The velocity profile in the viscous layer is a cubic function of distance.

Figs. 3–10 show the profiles of all the measured parameters, $\bar{v}$, v'_{rms}, $\bar{u}$, u'_{rms}, $\overline{T}$, T'_{rms}, $\overline{u'v'}$, $\overline{u'T'}$, $\overline{v'T'}$, k, in the boundary layer along the isothermal walls at $Y = 0.5$. In some of these figures, the present results are compared with past numerical results. The parameters are divided into three main groups (velocity field, temperature field and turbulence quantities).

3.2. Velocity field

The vertical velocity profile, $\bar{v}$, which defines the boundary layer increases steeply from the isothermal walls to a peak at $X = 0.007$ (5 mm) and then decreases rapidly to zero at about $X = 0.107$ (80 mm) from the hot wall, see Fig. 3(a). The profile of $\bar{v}$ near the cold wall is almost anti-symmetrical at mid-height of the cavity. The horizontal velocity profile, $\bar{u}$, is almost negligible in the boundary layer, see Fig. 3(a). In general, $\bar{u}$ is one order of magnitude smaller than $\bar{v}$. Fig. 3(a) also shows a comparison of the mean component of the vertical velocity at the cavity mid-height with the numerical simulation of Barozzi et al. [22] in an air filled cavity with $\mathrm{AR}_x = 1$ and $Ra = 10^{10}$. Also shown in the figure are the large-eddy simulation (LES) results of Peng and Davidson [23] in a similar cavity to the present study and under the same parameters. For the vertical velocity profile, the results of Barozzi et al. [22], which were based on the k–ε model, and that of Peng and Davidson [23] are generally in good agreement with the present results. However, from Fig. 3(a), it can be seen that the LES results of Peng and Davidson [23] marginally overestimated the peak value of the vertical velocity. Also, the results of Barozzi et al. [22] have a steeper velocity gradient near the wall and the location of the peak velocity is much closer to the wall than in the present study. Thus near the wall, the k–ε model predicts a higher rate of change of velocity which can lead to overestimation of the wall shear stress.

Fig. 3(b) shows that the vertical velocity fluctuations, v'_{rms}, and the horizontal velocity fluctuation, u'_{rms}, are concentrated in the boundary layer and decrease to almost nothing outside the boundary layer. One feature shown in Fig. 3(b) is the difference between u'_{rms} and v'_{rms}. The value of u'_{rms} is less than half that of v'_{rms} in the boundary layer at the cavity mid-height. On the whole, the profile of fluctuation quantities is anti-symmetric. Fig. 3(b) also shows a comparison of the fluctuation

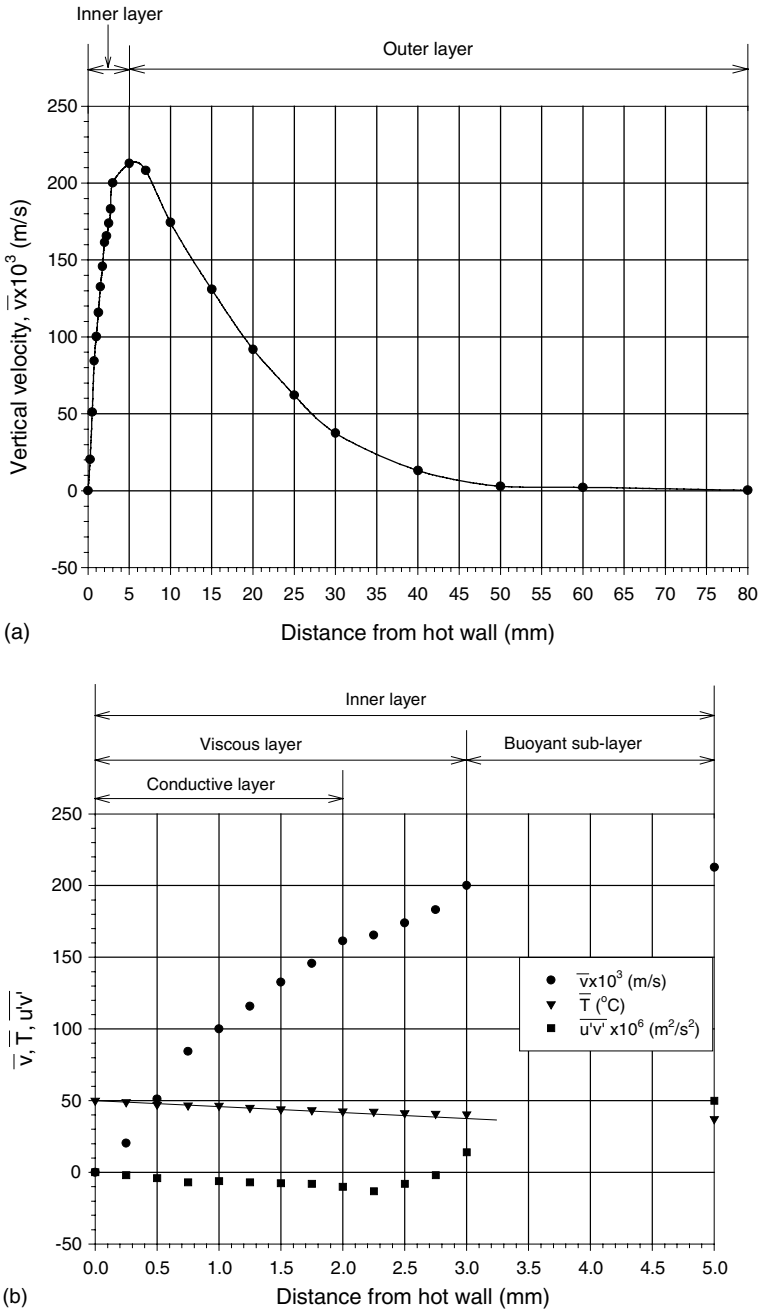

Fig. 2. Boundary layer structure at $Y = 0.5$: (a) vertical velocity profile near the hot wall and (b) inner boundary layer near the hot wall.

component of the vertical velocity at the mid-height of the cavity with the numerical simulation of Barozzi et al. [22] and the LES results of Peng and Davidson [23]. As noted above, the numerical simulation of Barozzi et al. [22] was based on the k–ε model, which assumed the local isotropy hypothesis, i.e. both the vertical and horizontal velocity fluctuations were assumed to be the same and were estimated by the following relationship:

$$v'_{\mathrm{rms}} = \sqrt{\frac{2k}{3}} \tag{9}$$

From Fig. 3(b), it can be seen that the experimental results are higher than the predicted values from the k–ε

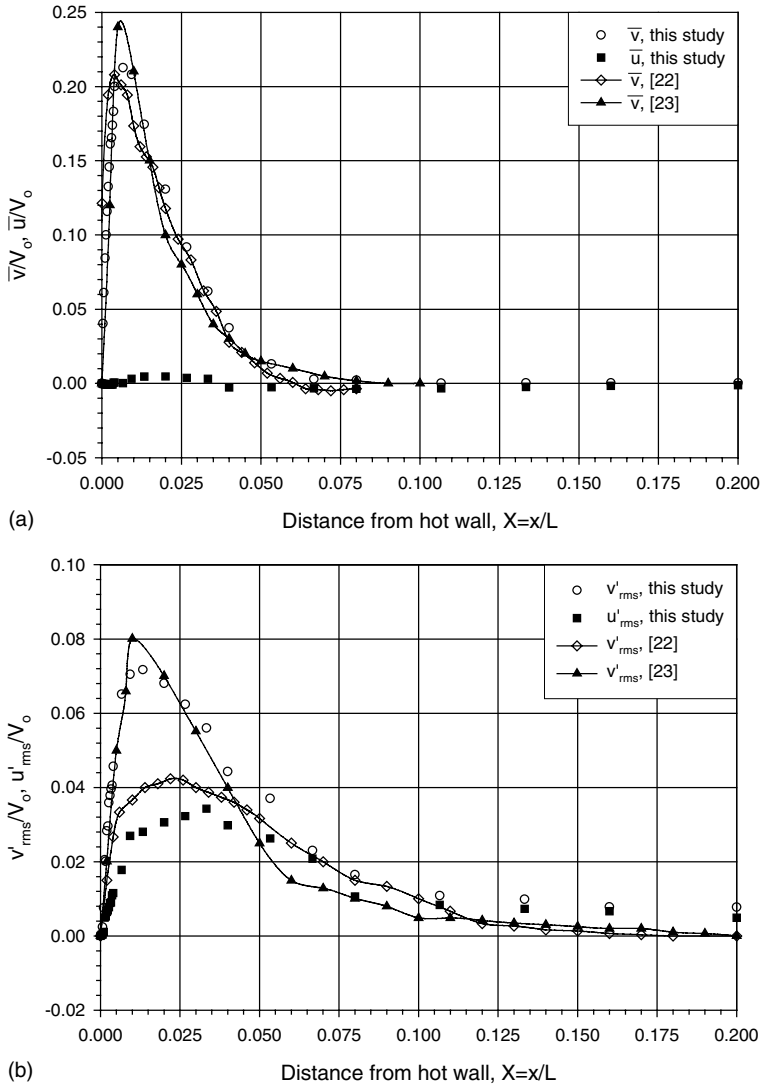

Fig. 3. Velocity field: (a) mean velocity at $Y = 0.5$ and (b) velocity fluctuation at $Y = 0.5$.

model of Barozzi et al. [22]. This is expected because the flow in the cavity is a wall shear flow and not isotropic and as such the vertical and horizontal velocity fluctuations are not expected to be the same. In the LES of Peng and Davidson [23], the subgrid-scale (SGS) stresses appearing in the filtered Navier–Stokes equations were responsible for the energy occurrence between the large-scale and the SGS eddies. They were modelled in alignment with the large-scale strain rate, $\overline{S}_{ij} = \frac{1}{2}\left(\frac{\partial \overline{u}_i}{\partial x_j} + \frac{\partial \overline{u}_j}{\partial x_i}\right)$, using the SGS eddy viscosity, ν_t, i.e.

$$\tau_{ij} = \overline{u'_i u'_j} - \overline{u'}_i \overline{u'}_j = -2\nu_t \overline{S}_{ij} + \frac{\delta_{ij}}{3}\tau_{kk} \tag{10}$$

By means of the gradient diffusion hypothesis, the SGS heat fluxes, h_j, in the filtered thermal energy equation were modelled as

$$h_j = \overline{T'}\,\overline{u'_j} - \overline{T'}\,\overline{u'}_j = -\alpha_t \frac{\partial \overline{T'}}{\partial x_j} \tag{11}$$

The SGS time scaling, T_{SGS}, took the following form:

$$T_{SGS} = \left(|\overline{S}|^2 - \frac{g\beta}{Pr_t}\frac{\partial \overline{T'}}{\partial x_j}\delta_{2j}\right)^{-1/2} \tag{12}$$

where the magnitude of the resolved local strain rate tensor, $|\overline{S}| = \sqrt{2\overline{S}_{ij}\overline{S}_{ij}}$. The present results agree reasonably well with the LES results of Peng and Davidson [23] except that the predicted values have a marginally higher peak and a thinner boundary layer structure. Fig. 3(b) confirms that on the whole, LES predicts turbulent quantities much better than k–ε models.

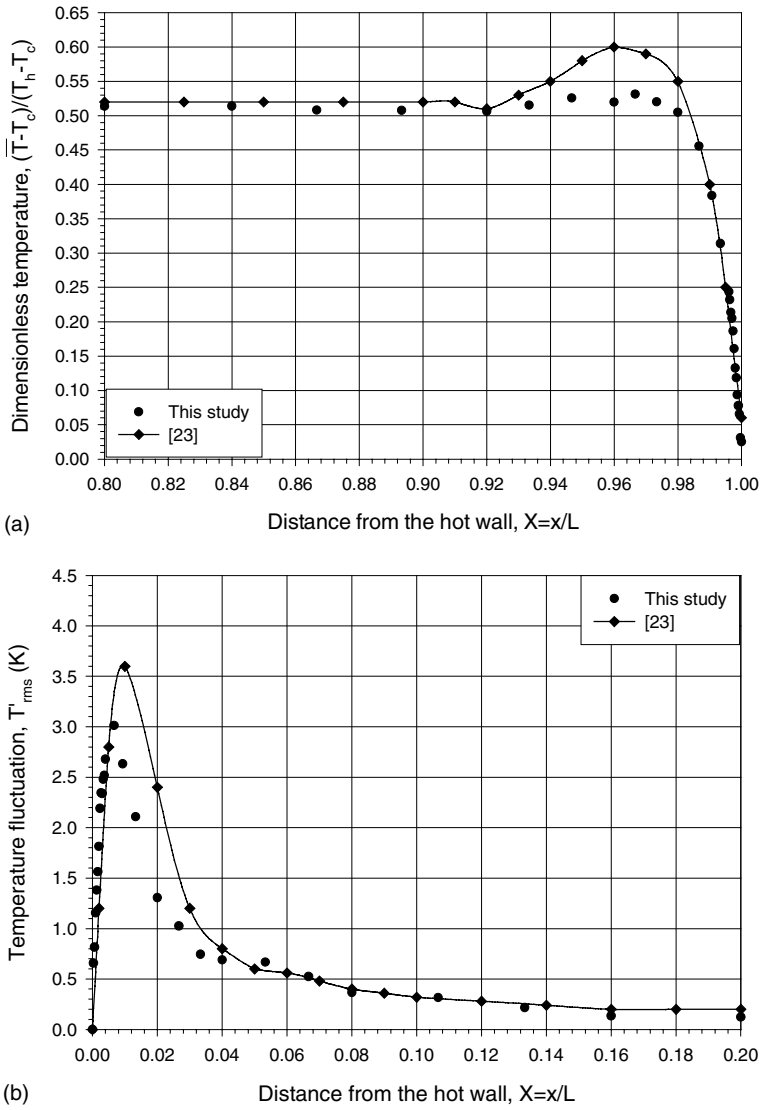

Fig. 4. Temperature field: (a) mean temperature at $Y = 0.5$ and (b) temperature fluctuation at $Y = 0.5$.

The flow in the present cavity was limited in the boundary layers along the walls. The velocity profile in the viscous layer was used to determine the wall shear stress. As stated earlier, in the viscous layer the velocity profile is a cubic function of distance from the wall, i.e.

$$\bar{v} = ax + bx^2 + cx^3 \tag{13}$$

where a, b and c can vary depending on height. Then the wall shear stress can be expressed as

$$\tau_w = \mu \left.\frac{\partial \bar{v}}{\partial x}\right|_{x=0} = a \tag{14}$$

Using the measured results in the viscous layer and a cubic polynomial least squares fitting process, an equation was obtained for the velocity profile. The equation was differentiated at $X = 0$ and 1 to obtain the velocity gradient and then the wall shear stress. The agreement of the shear stress values between the two isothermal walls is good, the largest difference being 0.08%, see Table 3.

3.3. Temperature field

Fig. 4(a) shows the temperature profile, $\overline{T}$, in the cold wall boundary layer at mid-height. The profile changes steeply near the isothermal wall. The temperature profile is nearly anti-symmetric in the hot wall boundary layer at mid-height. The authors present the cold wall data in Fig. 4(a) to allow comparison with the numerical work

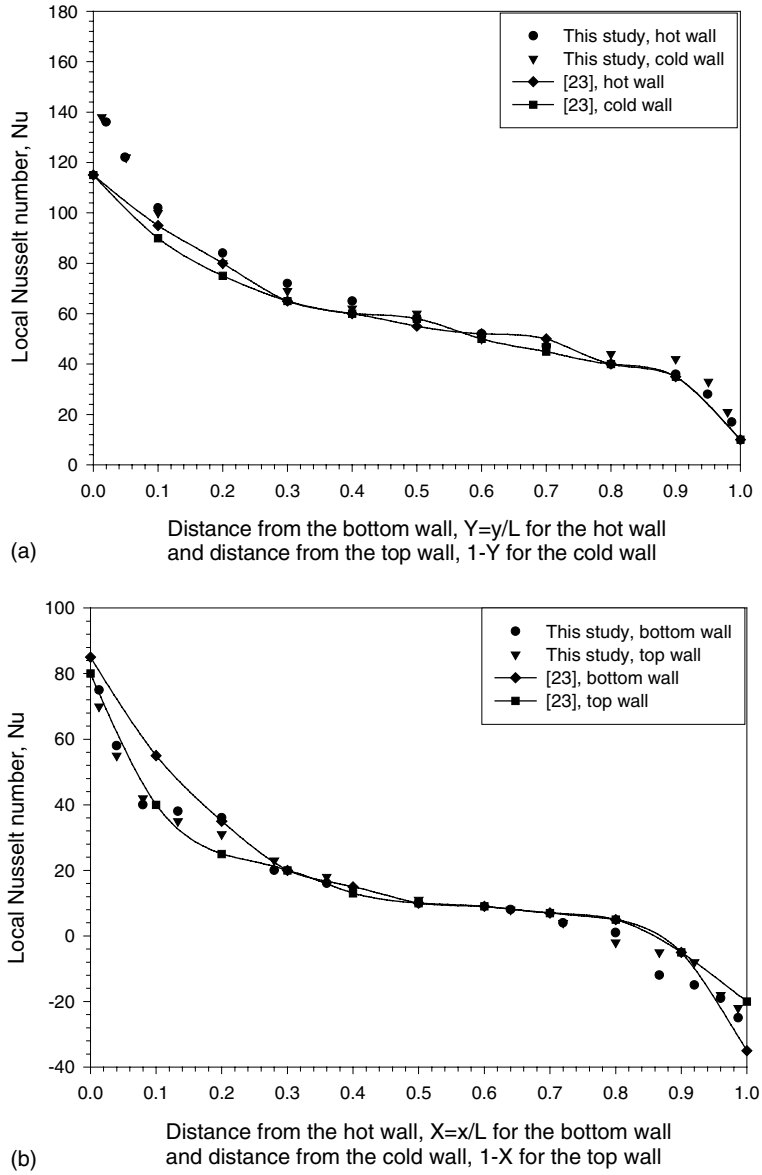

Fig. 5. Comparison of local Nusselt number: (a) local Nusselt number along the isothermal walls and (b) local Nusselt number along the horizontal walls.

of Peng and Davidson [23] who reported cold wall values. After an initial sharp decrease (from hot wall) and increase (from cold wall), the temperature remained fairly constant (from $X \sim 0.1$ to $X \sim 0.9$), indicating that the fluid in this region of the cavity was nearly stationary. The dimensionless temperature at the core of the cavity was 0.52 (30.7 °C), which is nearly equal to the mean temperature (and the ambient). This indicates that there was no heat loss through the passive vertical walls, i.e. through the guard cavities. The numerical results of Peng and Davidson [23] were obtained under the same parameters as the present study. Overall, the agreement between the present results for the mean temperature and the LES results of Peng and Davidson [23] is good in the cold wall boundary layer except that the temperature over-shoot is more pronounced in their case.

As seen in Fig. 4(b), the temperature fluctuation intensity increases with distance from the hot wall to a peak and then decreases to almost nothing. At mid-height the profile is almost symmetrical with a maximum value of around $T'_{\mathrm{rms}} = 3.0$ K near both the hot and cold walls. In general, the temperature fluctuation profile in

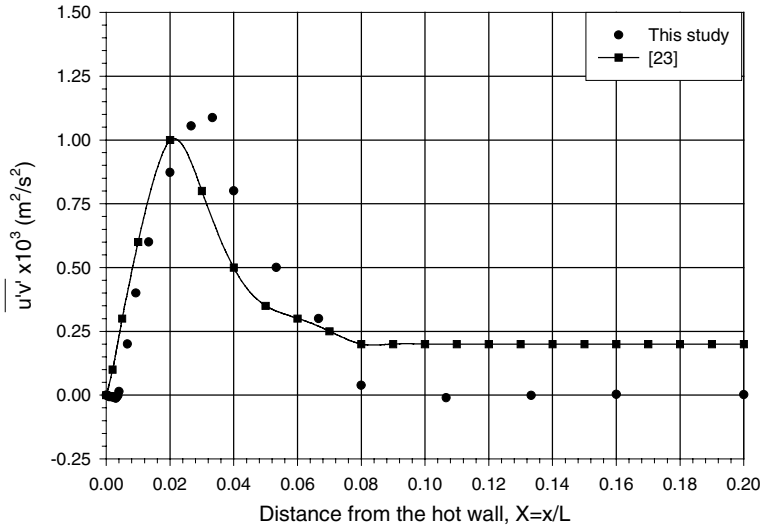

Fig. 6. Reynolds stress at $Y = 0.5$.

the cavity is nearly anti-symmetrical about the cavity centre. The present results are also compared with the numerical results of Peng and Davidson [23] in Fig. 4(b). The distribution of Peng and Davidson [23] has a higher peak value than in the present study but on the whole, the agreement between the present results and their results is good.

The local and average Nusselt numbers on the hot, cold, bottom and top walls can be determined using the measured temperature data in the thermal conductive boundary layer (see Fig. 2(b)) where the heat flux is constant as follows:

$$Nu_{\text{local}} = -\frac{L}{T_{\text{h}} - T_{\text{c}}} \frac{\partial \overline{T}}{\partial x_i}\bigg|_{\text{w}} \tag{15}$$

From this definition, the heat flux is positive with axis direction, i.e. the heat transfer from the hot wall into the cavity and from the cavity into the cold wall is positive. The heat transfer from the bottom wall into the cavity and from the cavity into the top wall is positive. The temperature gradient with respect to x or y was estimated by a linear best fitting from the first 6–9 measuring points near the wall. The local Nusselt numbers on the hot, cold, bottom and top walls of the cavity are presented in Table 6. The local Nusselt number reaches a maximum at the bottom of the hot wall and at the top of cold wall because of a thinner thermal boundary there. The measured maximum Nu number is about 138. At mid-height, the local Nusselt number is about 59. At the other end, because the fluid flow meets the wall, the heat transfer diminishes significantly and the local Nusselt number drops to about 20. The average Nusselt number was 62.9, 62.6, 13.9 and 14.4 for the hot, cold, bottom and top walls respectively. The local Nusselt number on the hot, cold, bottom and top walls in the cavity is compared with the numerical results of Peng and Davidson [23] at the same parameters as the present study in Fig. 5. On the lower part of the hot and cold walls, the simulation from Peng and Davidson [23] yields lower heat transfer rates than the present results (Fig. 5(a)). The agreement between the present results and that of Peng and Davidson [23] for the local Nusselt number along both the bottom and top walls of the cavity is good (Fig. 5(b)).

3.4. Turbulence quantities

The turbulence quantities obtained in this study are presented in Figs. 6–10. The Reynolds stress, $\overline{u'v'}$, near the hot wall is depicted in Fig. 6. For the first 3 mm form the wall the Reynolds stress in zero (see also Fig. 10(b)). The maximum positive value of $\overline{u'v'}$ is about 1.08×10^3 m^2/s^2 and 0.99×10^3 m^2/s^2 near the hot and cold walls respectively and is located well outside the maximum velocity point (5 mm or $X = 0.007$) at about 25 mm ($X = 0.033$) from the walls, see Fig. 6. This location coincides with the point where the intensities of velocity fluctuations become maximum in the outer layer. Thus, the outer layer has the same characteristics as the forced convection boundary layer because $\partial V/\partial x < 0$ and $\overline{u'v'} > 0$. The Reynolds stress is near zero between $X = 0.1$ and 0.9 at mid-height because outside the boundary layer the budget of $\overline{u'v'}$ are counter-balanced. Also, at mid-height the values of the Reynolds stress, $\overline{u'v'}$, near the two isothermal walls differ by about 8%. The dynamic viscosity of air is 17.62×10^{-6} N s/m^2 at 10 °C and 19.55×10^{-6} N s/m^2 at 50 °C, i.e. the 40 K temperature difference causes about 11% density differ-

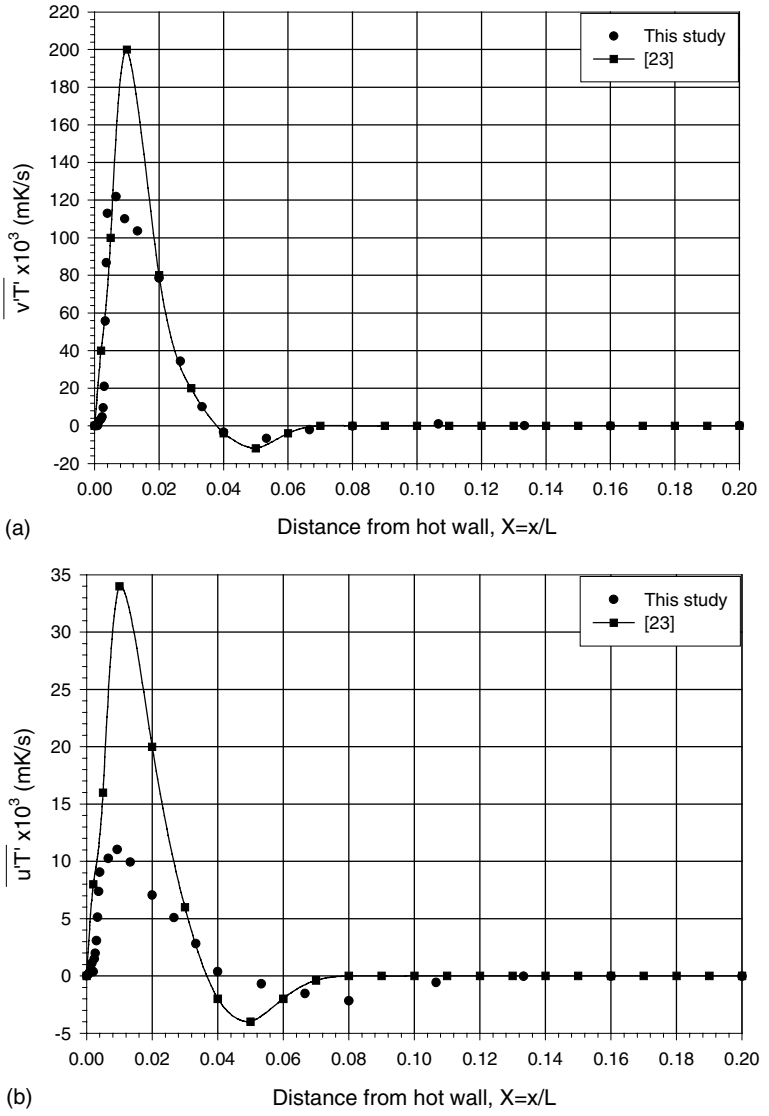

Fig. 7. Turbulent heat flux: (a) $Y = 0.5$ (vertical) and (b) $Y = 0.5$ (horizontal).

ence in the cavity and as such the Reynolds stress at mid-height can be considered to be symmetric. In Fig. 6, the Reynolds stress, $\overline{u'v'}$, at mid-height in the hot wall boundary layer of the cavity is also compared with the numerical results of Peng and Davidson [23] at the same *Ra* and aspect ratio. Overall, the agreement between the present results and that of Peng and Davidson [23] is poor. The numerical results of Peng and Davidson [23] have a relatively lower peak value, a narrow boundary layer structure and non-zero $\overline{u'v'}$ beyond $X = 0.1$.

The experimental results of $\overline{v'T'}$ and $\overline{u'T'}$, the turbulent heat fluxes in the *y*- and *x*-directions, at mid-height are shown in Fig. 7. At mid-height the values of $\overline{v'T'}$ near the two isothermal walls differ by about 9% and that of $\overline{u'T'}$ differ by about 12%. This is due to the change in value of the dynamic viscosity of air near the isothermal walls as explained above. Both $\overline{v'T'}$ and $\overline{u'T'}$ increase rapidly from the isothermal walls to a peak; $\overline{v'T'}$ peaks at about 0.121 and 0.110 m K/s near the hot and cold walls respectively. The corresponding values for $\overline{u'T'}$ are about 0.011 and 0.0097 m K/s. The peak value of the turbulent heat fluxes, $\overline{u_i'T'}$, is located in the vicinity of the maximum velocity location, which is about 5–7 mm from the walls, see Fig. 7. The turbulent heat fluxes are near zero between $X = 0.1$ and 0.9 at mid-height. In the overall boundary layer region, the fluctuating amplitude of $\overline{v'T'}$ far exceeds that of $\overline{u'T'}$ because of the large amplitude of the v' fluctuation, see Fig. 3(b). In general, the horizontal

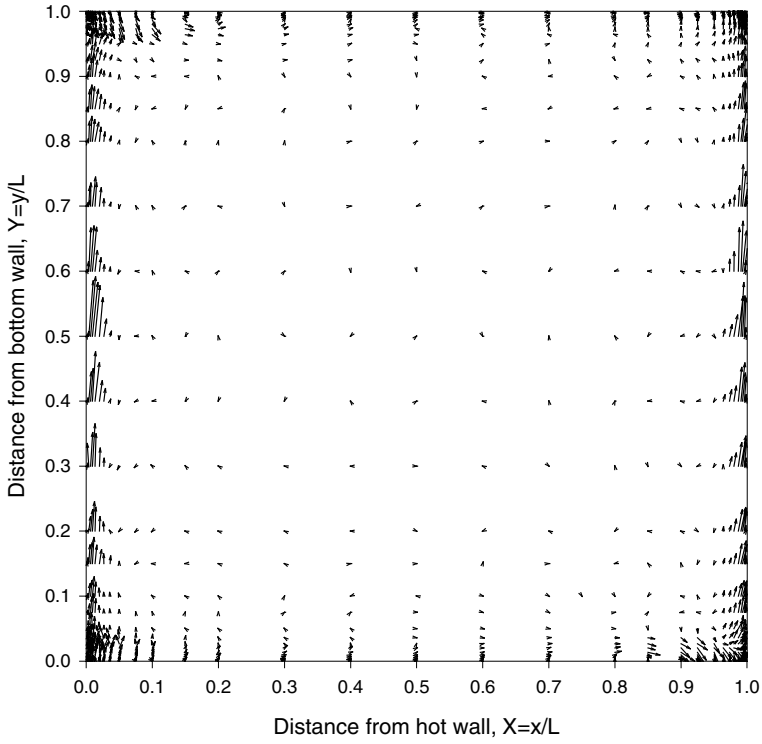

Fig. 8. Vector plot of the turbulent heat flux (scale: 0.0168 m K/s/mm).

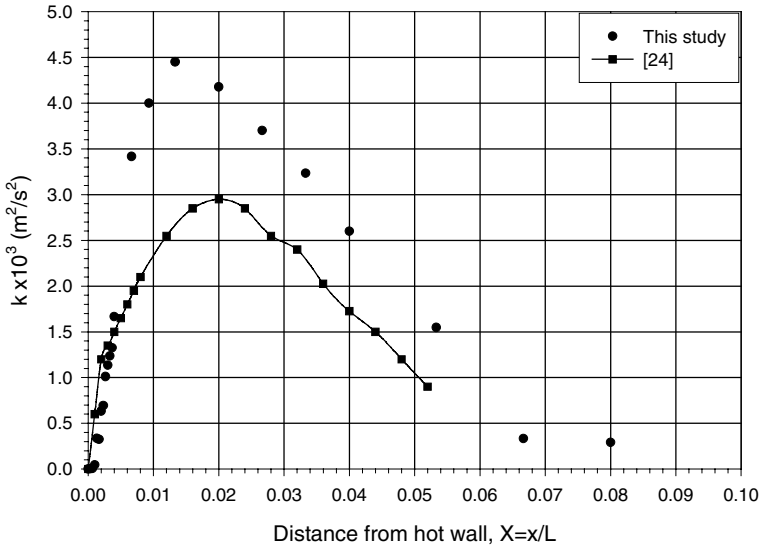

Fig. 9. Turbulent kinetic energy at $Y = 0.5$.

turbulent heat flux is one order of magnitude smaller than the vertical turbulent heat flux. The turbulent heat flux at mid-height in the cavity is compared in Fig. 7 with the numerical simulation of Peng and Davidson [23] at the same *Ra* and aspect ratio. For the vertical turbulent heat flux, the agreement between the two sets of results in terms of the boundary layer thickness is good but the simulation over-predicted the peak value

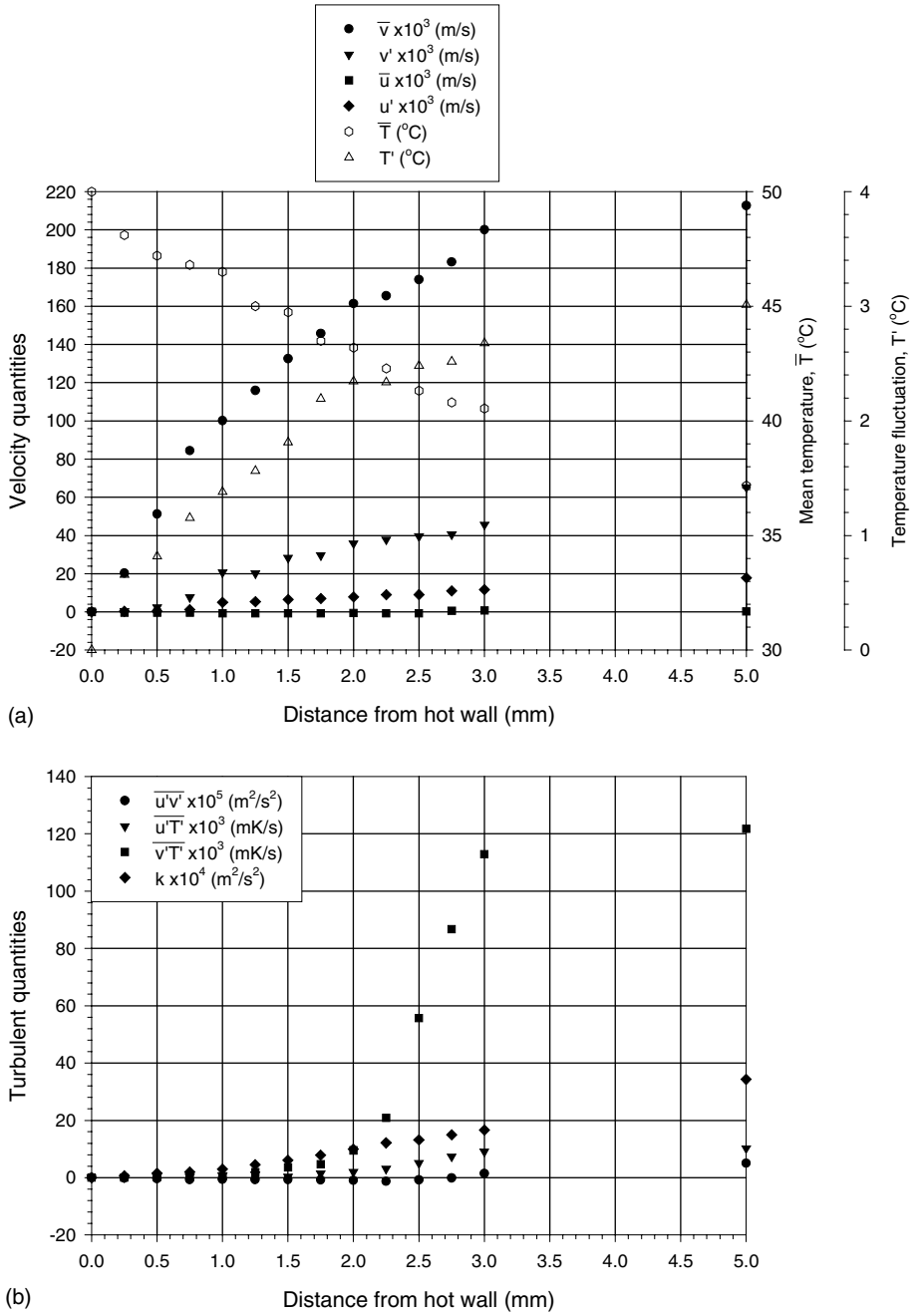

Fig. 10. Profiles of experimental parameters near the hot wall at $Y = 0.5$: (a) velocity and temperature quantities and (b) turbulent quantities.

by about 40% (Fig. 7(a)). In the case of the horizontal turbulent heat flux, the numerical simulation over-predicted the peak value by more than 67% (Fig. 7(b)). The whole turbulent heat flux vector plot in the cavity is given in Fig. 8. The turbulent heat flux vector is based on all the experimental data but is plotted on a mesh, which is coarser than the measurement mesh. This figure provides a very important insight into the structure of flow within the cavity. At the bottom of the hot wall (top of the cold wall) the turbulent heat flux is effectively zero. The absence of a turbulent heat flux in these regions suggests that the lower part of the hot wall (upper

part of the cold wall) boundary layer has many of the characteristics of a laminar flow. The figure also confirms that the majority of the turbulent heat flux is confined in a narrow strip along the isothermal walls.

The turbulent kinetic energy was estimated by Eq. (5) and the results at mid-height in the cavity are compared with the numerical results of Vasic and Hanjalic [24] using a low-*Re* number k–ε model at $Ra = 5 \times 10^{10}$ and $AR_x = 1$, see Fig. 9. Very close to the wall, the numerical predicted turbulent kinetic energy results of Vasic and Hanjalic [24] agree reasonably well with the present results. However, the predicted peak value in their case is much smaller and the boundary layer is also thinner than the measured one in the present study.

Fig. 10 shows the profiles of all the experimental parameters in the inner boundary layer of the hot wall at mid-height. The figure confirms what have been stated already in the above paragraphs, i.e. the horizontal velocity profile, $\bar{u}$, is one order of magnitude smaller than the vertical velocity profile, $\bar{v}$; the temperature profile, $\overline{T}$, changes steeply near the isothermal wall; the Reynolds stress, $\overline{u'v'}$, is near zero for the first 3 mm from the isothermal wall; etc. In addition to these findings, the figure shows that the horizontal velocity profile, $\overline{u}$, is almost negligible in the inner boundary layer. The value of the horizontal velocity fluctuation, u', is less than half that of the vertical velocity fluctuation, v'. Near the isothermal hot wall, the Reynolds stress, $\overline{u'v'}$, decreases to negligible values faster than its individual factors, u' and v'. Fig. 10(b) shows that in the conductive layer ($X < 2$ mm) the turbulent quantities are almost negligible, which confirms that the heat transfer in this region of the boundary layer is by pure conduction. Beyond this region to a greater part of the outer region, the heat transfer is by convection.

3.5. Turbulent diffusivity (α_t), turbulent viscosity (ν_t) and turbulent Prandtl number (Pr_t)

In the eddy viscosity model, one gives up the modeling of turbulent heat flux, $\overline{u_i'T'}$, and Reynolds stress, $\overline{u_i'u_j'}$, equations and adopts the generalized Boussinesq eddy viscosity model. Thus, the turbulent heat flux equation is given by

$$-\overline{u_i'T'} = \alpha_t \left(\frac{\partial \overline{T}}{\partial x_i} \right) \tag{16}$$

whereas the Reynolds stress equation is given by

$$-\overline{u_i'u_j'} = \nu_t \left(\frac{\partial \overline{u_i}}{\partial x_j} + \frac{\partial \overline{u_j}}{\partial x_i} \right) - \frac{2}{3}\delta_{ij}k \tag{17}$$

These hypotheses (Eqs. (16) and (17)) are valuable concepts, whose limitations should always be borne in mind. The turbulent diffusion hypothesis (Eq. (16)) implies that the scalar flux vector (in the present study temperature) is aligned with the mean scalar gradient vector. Even in simple turbulent flows this is found not to be the case. For example, in an experiment on homogeneous turbulent shear flow [25] the angle between $\nabla\overline{T}$ and $-\overline{u_i'T'}$ was measured to be 65°. Similarly, the turbulent viscosity hypothesis (Eq. (17)) implies that the anisotropy tensor, a_{ij}, is aligned with the mean rate of strain tensor, i.e.

$$a_{ij} \equiv \overline{u_i'u_j'} - \frac{2}{3}\delta_{ij}k = \nu_t \left(\frac{\partial \overline{u_i}}{\partial x_j} + \frac{\partial \overline{u_j}}{\partial x_i} \right) \tag{18}$$

Being symmetric and deviatoric, both a_{ij} and the mean rate of strain have five independent components. According to the turbulent viscosity hypothesis, these five components are related to each other through the scalar coefficient ν_t. Again, even in simple shear flow, it is found that this alignment does not occur [6]. An important class of flows consists of those that can be described by the two-dimensional turbulent boundary layer equations (of which the present study is an example). In the present study, the mean velocity is predominantly in the y-coordinate direction, while variations in mean quantities are predominantly in the x-coordinate direction. As a result of this, only one component ($\overline{v'T'}$) of the scalar flux and one Reynolds stress ($\overline{u'v'}$) appear in the boundary layer equations. Consequently, the turbulent diffusivity hypothesis reduces to

$$\overline{v'T'} = -\alpha_t \left(\frac{\partial \overline{T}}{\partial x} \right) \tag{19}$$

and the turbulent viscosity hypothesis to

$$\overline{u'v'} = -\nu_t \left(\frac{\partial \overline{v}}{\partial x} \right) \tag{20}$$

Both of these equations relate a single covariance to a single gradient. Providing that the covariance and the gradient have opposite signs—which is almost the case—then, rather than being hypotheses or assumptions, these equations can be taken as definitions of α_t and ν_t [6]. The distributions of the turbulent diffusivity and the turbulent viscosity close to the hot wall ($X = 0$–0.0333) at mid-height of the cavity is shown in Fig. 11. On the basis of the measured temperature and velocity results, these distributions were calculated using Eqs. (19) and (20). Using regression analysis, a polynomial equation was fitted to the measured mean data. The resulting best fit equation for the respective profile (temperature or velocity) was differentiated at the desired positions to obtain the temperature and velocity gradients. The turbulent diffusivity and viscosity data in Fig. 11 were made dimensionless by the kinematic viscosity of air.

The distribution of the turbulent Prandtl number, Pr_t, which is also shown in Fig. 11, is given by

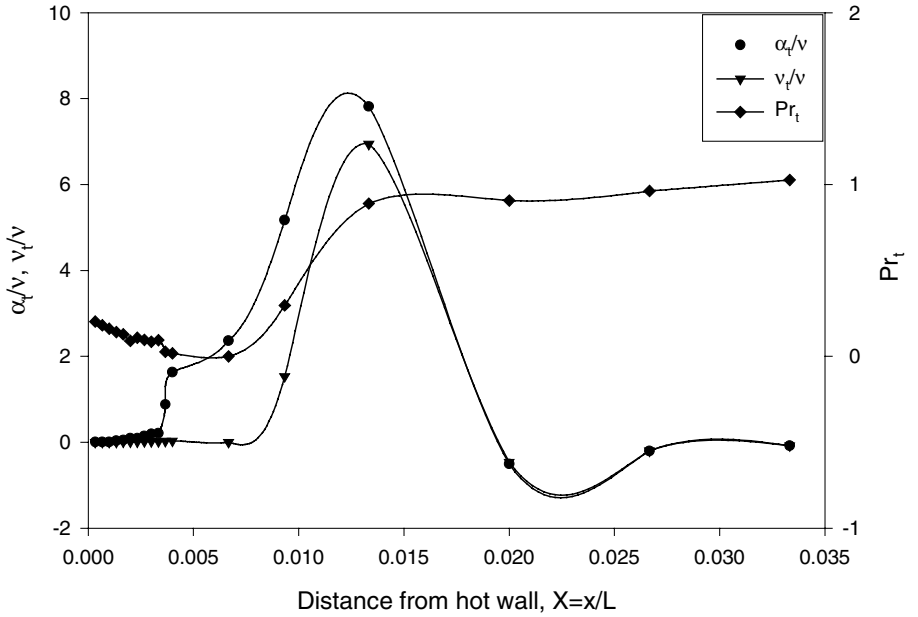

Fig. 11. Turbulent diffusivity, turbulent viscosity and turbulent Prandtl number.

$$Pr_t = \frac{\nu_t}{\alpha_t} \tag{21}$$

When considering the structure of turbulent heat transfer, these quantities are essentially important but have not been shown until now for a low level turbulent natural convection boundary layer along the isothermal walls of an air filled square cavity. As pointed out above, the concept of turbulent diffusivity and turbulent viscosity defined by Eqs. (19) and (20) is introduced under the condition that turbulent heat flux, $\overline{v'T'}$, or Reynolds stress, $\overline{u'v'}$, has a close relation with the mean temperature gradient or the mean velocity gradient. In the natural convection boundary layer, as shown in Fig. 10, Reynolds stress takes a very small value of almost zero near the wall, in the presence of a large mean velocity gradient and has a positive value at the maximum velocity location ($\partial\overline{v}/\partial x = 0$) without $\overline{u'v'}$ becoming zero. Therefore, the distribution of turbulent viscosity for momentum has a discontinuity at the maximum velocity location. On the other hand, turbulent diffusivity for heat shows a continuous profile. As a consequence, the distribution of turbulent Prandtl number defined as a ratio of turbulent viscosity and turbulent diffusivity also has a discontinuity at the maximum velocity location. The significance of introducing turbulent diffusivity, turbulent viscosity and turbulent Prandtl number is poor for the inner layer from the wall to the maximum velocity location. In the comparatively wide region ($X = 0.015$–0.03 of Fig. 11), turbulent viscosity and turbulent diffusivity have a similar profile and so the turbulent Prandtl number takes a value of about unity.

3.6. Dissipation rate of the temperature variance, ε_θ

In numerical studies, the strong coupling of the boundary layer and the cavity core flow makes computation very difficult for this wall bounded shear flow. Direct simulation of turbulent natural convection in a cavity is still too costly and numerical results from various k–ε models are not identical because the two-equation models cannot account correctly for the non-homogenous flow characteristics. Hanjalic et al. [26] proposed three- and four-equation models, k–ε–$\overline{T'^2}$ and k–ε–$\overline{T'^2}$–ε_θ, to solve this problem. Their results were compared with experimental data for Nusselt number, mean velocity and temperature. However, no comparison was made for the turbulent quantities, possibly due to the limitations of experimental data. The dissipation rate of the temperature variance, ε_θ, has the form

$$\begin{aligned}\varepsilon_\theta &= 2\alpha\overline{\left(\frac{\partial T'}{\partial x_i}\right)^2} \\ &= 2\alpha\left[\overline{\left(\frac{\partial T'}{\partial x}\right)^2} + \overline{\left(\frac{\partial T'}{\partial y}\right)^2} + \overline{\left(\frac{\partial T'}{\partial z}\right)^2}\right]\end{aligned} \tag{22}$$

where α is the fluid thermal diffusivity. This equation indicates that at least two-point measurements are needed for a direct experimental estimation. The dissipation rate of the temperature variance, ε_θ, in the cavity could not be measured directly in this study due to time constraint and as such, based on the measured temperature profiles in the cavity, an estimate would be made for this quantity near the isothermal walls ($\varepsilon_{\theta w}$) in this section.

Isotropic turbulent scalar fields have direction-independent mean-square scalar gradients due to the rotational symmetry. It is therefore sufficient for isotropic fields to measure only one of the three gradients (usually the streamwise gradient using Taylor's hypothesis), from which the scalar dissipation, ε_θ, is then given by the isotropic relation

$$\varepsilon_\theta = 6\alpha\overline{\left(\frac{\partial T'}{\partial x}\right)^2} \tag{23}$$

In this study, the flow is not 100% isotropic and as such a different approach will be used to estimate ε_θ. The temperature fluctuation profile very close to a wall of a 2D flow in cavities has no significant variation in the direction along the wall, see Fig. 12(a) and as such it can be expressed as follows (using Taylor's series):

$$T' = a_i x + b_i x^2 + \cdots \tag{24}$$

where the coefficients a_i and b_i are functions of time and their time averages are zero and x is distance from the wall. The dissipation rate of the temperature variance at the wall, $\varepsilon_{\theta w}$, can then be calculated from the experimental data using

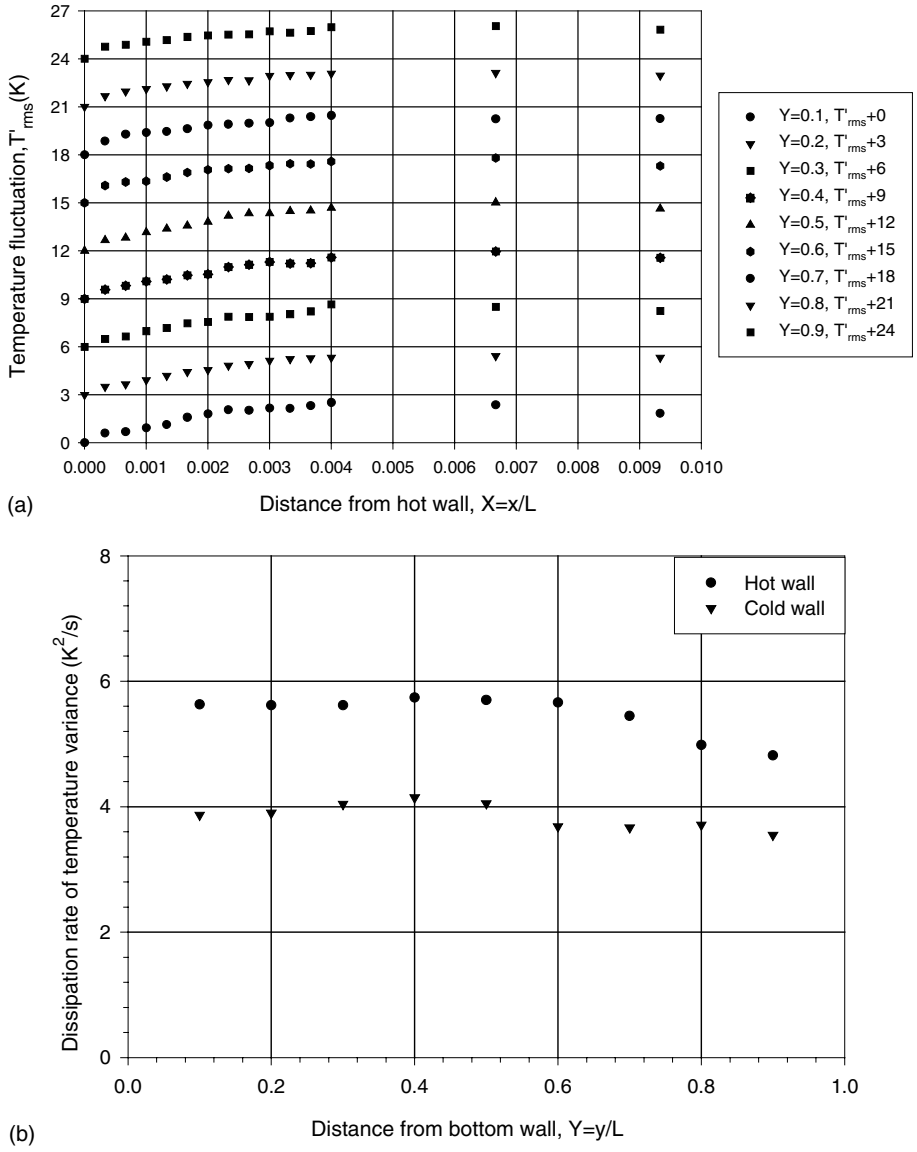

Fig. 12. Temperature fluctuation profiles with estimated dissipation rate of the temperature variance near the walls: (a) temperature fluctuation profiles at different heights near the hot wall and (b) estimated dissipation rate of the temperature variance near the walls.

$$\varepsilon_{\theta w} = 2\alpha\overline{\left(\frac{\partial T'}{\partial x}\right)^2}\bigg|_w \approx \frac{2\alpha}{N}\sum_{i=1}^{N} a_i^2 \approx 2\alpha\left(\frac{\partial T'_{rms}}{\partial x}\right)^2\bigg|_w \quad (25)$$

and

$$T'_{rms} = (\overline{T'^2})^{1/2} = \sqrt{\frac{1}{N}\sum_{i=1}^{M} T_i'^2} \quad (26)$$

where N in the number of readings taken in the experiments—10 000 in this study. The results based on the present measurements are shown in Fig. 12(b). The difference between the hot and cold walls is obvious; the average value for $\varepsilon_{\theta w}$ is 5.47 at the hot wall and 3.85 at the cold wall, i.e. 30% higher. It can be seen from this figure that for a major part of the walls the dissipation is nearly constant along the boundary layer. To the best of the authors' knowledge, this is the first experimental evidence relating to the dissipation rate of the temperature variance at a wall and could be useful for numerical modelling where $\overline{T'^2}$–ε_θ equations are involved.

4. Conclusions

The present study shows that for this kind of cavity the inner boundary layer along the isothermal walls is less than 7% of the outer boundary layer. Also, the viscous layer, which next to the isothermal walls, is about 3 mm (60% of the inner layer) with 2 mm of it being the conductive layer. The turbulent quantities are almost negligible in the conductive layer, which confirms that the heat transfer in this region of the boundary layer is by pure conduction. Overall, the local Nusselt number reaches a maximum at the bottom of the hot wall and at the top of the cold wall because of a thinner thermal boundary there.

The study also shows that at the bottom of the hot wall (top of the cold wall) the turbulent heat flux is effectively zero. The absence of a turbulent heat flux in these regions suggests that the lower part of the hot wall (upper part of the cold wall) boundary layer has many of the characteristics of a laminar flow. In general, the horizontal turbulent heat flux is one order of magnitude smaller than the vertical turbulent heat flux.

The turbulent diffusivity, turbulent viscosity and turbulent Prandtl number are essentially important quantities when considering the structure of turbulent heat transfer. However, as the present study has shown, the significance of introducing these quantities is limited for the inner layer, i.e. from the wall to the maximum velocity location. This is due to the fact that the distribution of turbulent viscosity for momentum has a discontinuity at the maximum velocity location and as such the distribution of turbulent Prandtl number defined as a ratio of turbulent viscosity and turbulent diffusivity also has a discontinuity at this location. However, beyond the maximum velocity location, turbulent viscosity and turbulent diffusivity have a similar profile and so the turbulent Prandtl number takes a value of about unity.

From the above comparison and discussion, it can be stated that the k–ε model and LES can predict the mean quantities such as velocity and temperature in the present cavity reasonably well but cannot predict the fluctuation and turbulence quantities. LES predicts the flow quantities much better than the k–ε model. The results described in this paper were obtained with high precision and can be useful as benchmark data for comparison with CFD codes. Such numerical simulation should include realistic boundary conditions at the top and bottom horizontal walls as given in this study.

References

[1] M.W. Nansteel, R. Grief, Natural convection in enclosures with two- and three-dimensional partitions, Int. J. Heat Mass Transfer 27 (4) (1984) 561–571.
[2] D.A. Olson, L.R. Glicksman, H.M. Ferm, Steady-state natural convection in empty and partitioned enclosures at high Rayleigh numbers, ASME J. HT 112 (1990) 640–647.
[3] F. Penot, A. N'Dame, Successive bifurcations of natural convection in a vertical enclosure heated from the side, in: Heat Transfer, Third UK National Conference Incorporating First European Conference on Thermal Sciences, Birmingham, UK, vol. 1, 1992, pp. 507–513.
[4] Y.S. Tian, T.G. Karayiannis, Low turbulence natural convection in an air filled square cavity, Part I: Thermal and fluid flow fields, Int. J. Heat Mass Transfer 43 (2000) 849–866.
[5] Y.S. Tian, T.G. Karayiannis, Low turbulence natural convection in an air filled square cavity, Part II: The turbulence quantities, Int. J. Heat Mass Transfer 43 (2000) 867–884.
[6] S.B. Pope, Turbulent Flows, Cambridge University Press, 2000.
[7] B.E. Launder, B.I. Sharma, Application of the energy dissipation model of turbulence to the calculation of flow near a spinning disc, Letters in Heat and Mass Transfer 1 (2) (1974) 131–138.
[8] T. Cebeci, P. Bradshaw, Physical and Computational Aspects of Convective Heat Transfer, Springer-Verlag, Berlin, 1988.
[9] H.P. Kreplin, H. Eckelmann, Behaviour of the three fluctuating velocity components in the wall region of a turbulent channel flow, Fluid 22 (1979) 1233–1239.
[10] P.R. Spalart, Direct simulation of a turbulent boundary layer up to $R_\theta = 1410$, J. Fluid Mech. 187 (1988) 61–98.
[11] S. Mergui, F. Penot, Natural convection in a differentially heated square cavity: experimental investigation at $Ra_H = 1.69 \times 10^9$, Int. J. Heat Mass Transfer 39 (3) (1996) 563–574.
[12] F. Ampofo, Turbulent natural convection in an air filled standard or partitioned square cavity, PhD Thesis, South Bank University, December 2001.

[13] S. Mergui, F. Penot, J.L. Tuhault, Experimental natural convection in an air-filled square cavity at $Ra_H = 1.7 \times 10^9$, in: R.A.W.M. Henkes, C.J. Hoogendoorn (Eds.), Turbulent Natural Convection in Enclosures—A Computational and Experimental Benchmark Study, Proceedings of the Eurotherm Seminar No. 22, Delft, The Netherlands, March 25–27, 1992, pp. 97–108.

[14] A.M. Lankhorst, Laminar and turbulent natural convection in cavities—numerical modelling and experimental validation, PhD Thesis, Technology University of Delft, 1991.

[15] C. Beghein, F. Allard, A. Draoui, Numerical modelling of turbulent convection in a thermally-driven square cavity, in: R.A.W.M. Henkes, C.J. Hoogendoorn (Eds.), Turbulent Natural Convection in Enclosures—A Computational and Experimental Benchmark Study, Proceedings of the Eurotherm Seminar No. 22, Delft, The Netherlands, March 25–27, 1992, pp. 31–42.

[16] S. Ziai, Turbulent natural convection in a large rectangular air cavity, PhD Thesis, Queen Mary College, University of London, 1983.

[17] K.J. King, Turbulent natural convection in rectangular air cavities. PhD Thesis, Queen Mary College, University of London, 1989.

[18] S. Paolucci, Direct numerical simulation of two-dimensional turbulent natural convection in an enclosed cavity, J. Fluid Mech. 215 (1990) 229–262.

[19] I.N.G. Wardana, T. Ueda, M. Mizomoto, Velocity–temperature correlation in strongly heated channel flow, Exp. Fluids 18 (1995) 454–461.

[20] W.K. George, S.P. Capp, A theory for natural convection turbulent boundary layer next to heated vertical surfaces, Int. J. Heat Mass Transfer 22 (1979) 813–826.

[21] J.T. Davies, Turbulence Phenomena, Academic Press, New York, 1972.

[22] G.S. Barozzi, E. Nobile, A.C.M. Sousa, Contribution to the numerical simulation of turbulent natural convection in rectangular enclosures, in: R.A.W.M. Henkes, C.J. Hoogendoorn (Eds.), Turbulent Natural Convection in Enclosures—A Computational and Experimental Benchmark Study, Proceedings of the Eurotherm Seminar No. 22, Delft, The Netherlands, March 25–27, 1992, pp. 19–30.

[23] S.H. Peng, L. Davidson, Numerical investigation of turbulent buoyant cavity flow using LES, in: 3rd International Symposium on Turbulence, Int. J. Heat Mass Transfer (2000) 1–8.

[24] S. Vasic, K. Hanjalic, Turbulent natural convection in a square cavity—benchmark computations, in: R.A.W.M. Henkes, C.J. Hoogendoorn (Eds.), Turbulent Natural Convection in Enclosures—A Computational and Experimental Benchmark Study, Editions Europeennes Thermique et Industrie, 1993, pp. 133–144.

[25] S. Tavoularis, S. Corrsin, Experiments in nearly homogeneous turbulent shear flow with a uniform mean temperature gradient, Part 1, Fluid Mech. 104 (1981) 311–347.

[26] K. Hanjalic, S. Kenjeres, F. Durst, Natural convection in partitioned two-dimensional enclosures at higher Rayleigh number, Int. J. Heat Mass Transfer 39 (7) (1996) 1407–1427.